August 1983

# Atomic Photoionization

Anthony F. Starace
*University of Nebraska-Lincoln*, astarace1@unl.edu

Published in FUNDAMENTAL PROCESSES IN ENERGETIC ATOMIC COLLISIONS
Edited by H. O. Lutz, J. S. Briggs, & H. Kleinpoppin
New York : Published in cooperation with NATO Scientific Affairs Division by Plenum Press, 1983.

# ATOMIC PHOTOIONIZATION

Anthony F. Starace

Behlen Laboratory of Physics
The University of Nebraska
Lincoln, Nebraska 68588-0111, U.S.A.

## INTRODUCTION

We present here a brief overview of the theory of atomic photoionization. The main aim is to describe current theoretical understanding of the dynamics of the photon-atom collision process. In particular the discussion focuses on those kinds of electron correlation that have been found to be most important for photoionization processes. The general theoretical formulation of the interaction between an incident photon and an N-electron atom is presented first. This is followed by a description of those quantitative and qualitative features of the photoionization cross section that can be understood within a central potential model. The particle-hole type of electron correlations are then discussed in detail, as they are by far the most important for describing the single photoionization of closed-shell atoms near ionization thresholds. Among recent developments, we discuss in some detail the hyperspherical coordinate method for obtaining correlated two-electron wavefunctions. Not only has the method provided a novel means for classifying whole series of doubly excited states, but it has also provided a new interpretation of the process of photoionization accompanied by excitation. More detailed presentations of the theory of atomic photoionization have been given by the author elsewhere.[1-3]

## GENERAL CONSIDERATIONS

### The Interaction Hamiltonian

Consider an N-electron atom with nuclear charge Z. In nonrelativistic approximation it is described by the Hamiltonian

$$H = \sum_{i=1}^{N} \left\{ \frac{p_i^2}{2m} - \frac{Ze^2}{r_1} \right\} + \sum_{i>j=1}^{N} \frac{e^2}{|\vec{r}_i - \vec{r}_j|} \tag{1}$$

In Eq. (1) the one-electron terms in brackets describe the kinetic and potential energy of each electron in the Coulomb field of the nucleus; the second set of terms describe the repulsive electrostatic potential energy between electron pairs. The interaction of this atom with external electromagnetic radiation is described by the additional terms obtained upon replacing $\vec{p}_i$ by $\vec{p}_i + \frac{|e|}{c}\vec{A}(\vec{r}_i, t)$, where $\vec{A}(\vec{r}_i, t)$ is the vector potential for the radiation. The interaction Hamiltonian is thus

$$H_{int} = \sum_{i=1}^{N} \left\{ \frac{+|e|}{2mc} (\vec{p}_i \cdot \vec{A}(\vec{r}_i,t) + \vec{A}(\vec{r}_i,t) \cdot \vec{p}_i) + \frac{e^2}{2mc^2} |\vec{A}(\vec{r}_i,t)|^2 \right\} \tag{2}$$

Under the most common circumstance of single-photon ionization of an outer-subshell electron, the interaction Hamiltonian in (2) may be simplified considerably. Firstly we note that the third term in (2) may be dropped, as it introduces two-photon processes since it is of second order in $\vec{A}$. In any case it is small compared to single photon processes since it is of second order in the coupling constant $|e|/c$. Secondly we choose the Coulomb gauge for $\vec{A}$, which fixes the divergence of $\vec{A}$ as $\vec{\nabla} \cdot \vec{A} = 0$. $\vec{A}$ thus describes a transverse radiation field. Furthermore $\vec{p}$ and $\vec{A}$ now commute and hence the first and second terms in (2) may be combined. Thirdly, we introduce the following form for $\vec{A}$:

$$A(r_i,t) = \left( \frac{2\pi c^2 \hbar}{\omega V} \right)^{\frac{1}{2}} \hat{\epsilon}\, e^{i(\vec{k} \cdot r_i - \omega t)} \tag{3}$$

This classical expression for $\vec{A}$ may be shown[4] to give photoabsorption transition rates that are in agreement with those obtained using the quantum theory of radiation. Here $\vec{k}$ and $\omega$ are the wave vector and angular frequency of the incident radiation, $\hat{\epsilon}$ is its polarization unit vector, and V is the spatial volume. Fourthly, we note that the electric dipole approximation, in which $\exp i(\vec{k} \cdot \vec{r}_i)$ is replaced by unity, is usually appropriate. The

radius $r_i$ of the atomic electrons is usually of order 1 Å. Thus for $\lambda \gg 100$ Å, $|\vec{k} \cdot \vec{r}_i| \ll 1$. Now $\lambda \gg 100$ Å corresponds to photon energies $\hbar\omega \ll 124$ eV. For outer atomic subshells, the bulk of the photoabsorption occurs for much smaller photon energies thus validating the use of the electric dipole approximation. This approximation cannot be used uncritically, however, as we shall discuss later. Use of all of the above conventions and approximations allows us to reduce $H_{int}$ in Eq. (2) to the following simplified form:

$$H_{int} = \frac{+|e|}{mc} \left( \frac{2\pi c^2 \hbar}{\omega V} \right)^{\frac{1}{2}} \sum_{i=1}^{N} \hat{\varepsilon} \cdot \vec{p}_i \exp(-i\omega t) \tag{4}$$

$H_{int}$ thus has the form of a harmonically time-dependent perturbation. According to time-dependent perturbation theory the photoionization cross section is proportional to the matrix element of (4) between the initial and final electronic states described by the atomic Hamiltonian in (1), as we shall see below. In what follows we shall for simplicity adopt atomic units in which $|e| = m = \hbar = 1$.

Alternative Forms for the Transition Matrix Element

One sees that the matrix element of (4) is proportional to the matrix element of the momentum operator $\sum_i \vec{p}_i$. Alternative expressions for this matrix element may be obtained from the following operator equations involving commutators of the exact atomic Hamiltonian in (1):

$$\sum_{i=1}^{N} \vec{p}_i = -i \left[ \sum_{i=1}^{N} \vec{r}_i, H \right] \tag{5a}$$

$$\left[ \sum_{i=1}^{N} p_i, H \right] = -i \sum_{i=1}^{N} \frac{Z\vec{r}_i}{r_i^3} \tag{5b}$$

Matrix elements of (5) between energy eigenstates $\langle \psi_0|$ and $|\psi_f\rangle$ of the Hamiltonian (1) having energies $E_0$ and $E_f$ respectively give:

$$\langle \psi_0 | \sum_{i=1}^{N} \vec{p}_i | \psi_f \rangle = -i\omega \langle \psi_0 | \sum_{i=1}^{N} \vec{r}_i | \psi_f \rangle \tag{6a}$$

$$< \psi_0 | \sum_{i=1}^{N} \vec{p}_i | \psi_f > = \frac{-i}{\omega} < \psi_0 | \sum_{i=1}^{N} \frac{Z\vec{r}_i}{r_i^3} | \psi_f > \qquad (6b)$$

where

$$\omega = E_f - E_0 \, . \qquad (6c)$$

Matrix elements of $\sum_{i=1}^{N} \vec{p}_i$, $\sum_{i=1}^{N} \vec{r}_i$, and $\sum_{i=1}^{N} \frac{Z\vec{r}_i}{r_i^3}$ are known simply as the "velocity," "length," and "acceleration" forms of the electric dipole matrix element.

As emphasized by Chandrasekhar,[5] equality of the matrix elements in (6) does not hold when approximate eigenstates of the N-electron Hamiltonian in (1) are used. In such a case qualitative considerations may help to determine which matrix elements are most reliable. One may note, for example, that the length form tends to emphasize the large r part of the approximate wavefunctions, that the acceleration form tends to emphasize the small r part of the wavefunctions, and that the velocity form tends to emphasize intermediate values of r.

If instead of employing approximate eigenstates of the exact N-electron Hamiltonian one employs exact eigenstates of an approximate N-electron Hamiltonian, then one may show that inequality of the matrix elements in (6) is a measure of the non-locality of the potential in the approximate Hamiltonian.[6] The exchange part of the Hartree-Fock potential is an example of such a non-local potential. Non-local potentials are also implicitly introduced in configuration interaction calculations employing a finite number of configurations.[6] One may eliminate the ambiguity of which form of the electric dipole transition operator to use by requiring that the Schrödinger equation for the atom described by an approximate non-local potential be gauge invariant. Only the length form of the electric dipole transition operator is consistent with gauge invariance of the approximate Schrödinger Equation.[6]

Two further points regarding the alternative forms of the electric dipole transition operator should be noted. Firstly, when one uses an approximate local potential to describe the N-electron atom, as in a central potential model, then matrix elements of the three alternative forms for the electric dipole operator are strictly equal. Since central potential model cross sections may differ from experiment by a factor of two or more near outer shell ionization thresholds, one sees that equality of the alternative forms for the transition matrix element should not in itself be taken to indicate the accuracy of the calculated

results. Secondly, one can show that in the random phase approximation, which does generally give accurate cross sections for single photoionization of closed shell atoms, the length and velocity matrix elements are strictly equal.[7] No general prescription exists, however, for ensuring that the length and velocity matrix elements are equal at each level of approximation to the exact N-electron Hamiltonian.

## Selection Rules

If one ignores relativistic interactions for simplicity, then a general atomic photoionization process may be described in LS-coupling as follows:

$$A(L,S,M_L,M_S,\pi_A) + \gamma(\pi_\gamma,\ell_\gamma,m_\gamma) \longrightarrow$$

$$A^+(\bar{L}\,\bar{S}\,\pi_{A^+})\,\varepsilon\ell\,(L',\,S',\,M_{L'},\,M_{S'}) \qquad (7)$$

Here the atom A is ionized by the photon $\gamma$ to produce a photoelectron with kinetic energy $\varepsilon$ and orbital angular momentum $\ell$. The photoelectron is coupled to the ion $A^+$ with total orbital and spin angular momenta L' and S'. In the electric dipole approximation the photon may be regarded as having odd parity, i.e., $\pi_\gamma = -1$, and unit angular momentum, i.e., $\ell_\gamma = 1$. This is obvious from Eq. (6), where the electric dipole operator is seen to be a vector operator. The component $m_\gamma$ of the photon in the electric dipole approximation is $\pm 1$ for right or left circularly polarized light and 0 for linearly polarized light. Angular momentum and parity selection rules for the electric dipole transition in (7) imply the following relations between the initial and final state quantum numbers:

$$L' = L \oplus a = \bar{L} \oplus \ell \qquad (8a)$$

$$M_{L'} = M_L + m_\gamma = M_{\bar{L}} + m_\ell \qquad (8b)$$

$$S' = S = \bar{S} \oplus \tfrac{1}{2} \qquad (8c)$$

$$M_{S'} = M_S = M_{\bar{S}} + m_s \qquad (8d)$$

$$\Pi_A\,\Pi_{A^+} = (-1)^{\ell+1} \qquad (8e)$$

Note that in Eq. (8e) we have used the fact that the parity of the photoelectron is $(-1)^\ell$. Note also that the direct sum symbol $\oplus$ implies that two vectors A and B are added together vectorially, i.e., $A \oplus B = A + B,\ A + B - 1,\ \cdots,\ |A - B|$.

An important theoretical concept is that of the channel. In the process indicated in (7) the quantum numbers $\alpha \equiv \bar{L}, \bar{S}, \pi_{A^+}, \ell, L', S', M_{L'}$ and $M_{S'}$ (plus any other quantum numbers needed to uniquely specify the state of the ion $A^+$) define a final state channel. Note that all final states that differ only in the photoelectron energy $\varepsilon$ belong to the same channel. Note also that the quantum numbers $L', S', M_{L'}, M_{S'}$, and $\pi_{TOTAL} = (-1)^{\ell}\pi_{A^+}$ are the only good quantum numbers for final states described by the N-electron Hamiltonian in (1). This Hamiltonian thus mixes final state channels having the same angular momentum and parity quantum numbers but differing quantum numbers for the ion and the photoelectron, i.e., differing $\bar{L}, \bar{S}$, and $\ell$ but the same $L', S', M_{L'}, M_{S'}$ and $(-1)^{\ell}\pi_{A^+}$.

Boundary Conditions on the Final State Wavefunction

Theoretical photoionization calculations obtain final state wavefunctions satisfying the asymptotic boundary condition that the photoelectron is ionized in channel $\alpha$. Mathematically this boundary condition is expressed as follows:

$$\psi^-_{\alpha E}(\vec{r}_1\vec{s}_1,\cdots\vec{r}_N\vec{s}_N) \xrightarrow[r_N\to\infty]{} \theta_\alpha(\hat{r}_1\vec{s}_1,\cdots\hat{r}_N\vec{s}_N)\,\frac{1}{i(2\pi k_\alpha)^{1/2}}\,\frac{1}{r_N}\exp(i\Delta_\alpha)$$

$$-\sum_{\alpha'}\theta_{\alpha'}(\hat{r}_1\vec{s}_1,\cdots\hat{r}_N\vec{s}_N)\,\frac{1}{i(2\pi k_{\alpha'})^{1/2}}\,\frac{1}{r_N}\exp(-i\Delta_{\alpha'})\,S^\dagger_{\alpha'\alpha} \qquad (9a)$$

where the phase appropriate for a Coulomb field is:

$$\Delta_\alpha \equiv k_\alpha r_N - \tfrac{1}{2}\pi\ell_\alpha + \frac{1}{k_\alpha}\log 2k_\alpha r_N + \sigma_{\ell_\alpha} \qquad (9b)$$

The minus superscript on the wavefunction in (9a) indicates the so-called "incoming wave" normalization: i.e., asymptotically $\psi^-_{\alpha E}$ has outgoing spherical Coulomb waves only in channel $\alpha$ whereas there are incoming spherical Coulomb waves in all channels. $S^\dagger_{\alpha'\alpha}$ is the Hermitian conjugate of the S-matrix of scattering theory. $\theta_\alpha$ indicates the coupled wavefunction of the ion and the angular and spin parts of the photoelectron's wavefunction. $k_\alpha$ is the photoelectron's momentum in channel $\alpha$ and $\ell_\alpha$ is its orbital angular momentum. $\sigma_{\ell_\alpha}$ in (9b) is the Coulomb phase shift.

While theoretically one calculates channel functions $\psi^-_{\alpha E}$, experimentally one measures photoelectrons which asymptotically have well defined linear momentum $\vec{k}_\alpha$ and well-defined spin state $m_{s_\alpha}$, and ions in well-defined states $\bar{\alpha} \equiv \bar{L}\ \bar{S}\ M_{\bar{L}}\ M_{\bar{S}}$. The wavefunction appropriate for this experimental measurement is related to the theoretical channel functions by uncoupling the ionic and electronic orbital and spin angular momenta and projecting the photoelectron's angular momentum states $\ell_\alpha$, $m_\alpha$ onto the direction $\hat{k}_\alpha$ by means of the spherical harmonic $Y^*_{\ell_\alpha m_\alpha}(\hat{k}_\alpha)$. One may show that this relation is[1]

$$\psi^-_{\bar{\alpha}\vec{k}_\alpha}(\vec{r}_1\vec{s}_1,\cdots,\vec{r}_N\vec{s}_N) = \sum_{\ell_\alpha m_\alpha} \frac{i^{\ell_\alpha}\exp(-i\,\sigma_{\ell_\alpha})}{k_\alpha^{1/2}}\, Y^*_{\ell_\alpha m_\alpha}(\hat{k}_\alpha)$$
$$\times \sum_{LM_L} \langle \bar{L}M_{\bar{L}}\,\ell_\alpha m_\alpha | LM_L\rangle \sum_{SM_S} \langle \bar{S}M_{\bar{S}}\,\tfrac{1}{2}m_{s_\alpha}|SM_S\rangle \psi^-_{\alpha E}(\vec{r}_1\vec{s}_1,\cdots,\vec{r}_n\vec{s}_N). \tag{10}$$

In Eq. (10) the coefficients in brackets are Clebsch-Gordan coefficients. The wavefunction in (10) is also normalized to a delta function in momentum space, i.e.,

$$\int (\psi^-_{\bar{\alpha}\vec{k}_\alpha})^\dagger\, \psi^-_{\bar{\alpha}',\vec{k}_{\alpha'}}\, d^3\vec{r} = \delta_{\bar{\alpha}\bar{\alpha}'}\,\delta(k_\alpha - k_{\alpha'}) \tag{11}$$

The factors $i^{\ell_\alpha}\exp(-i\sigma_{\ell_\alpha})k_\alpha^{-1/2}$ ensure that for large $r_N$ Eq. (10) represents a Coulomb wave with momentum $\vec{k}_\alpha$ times the ionic wavefunction for the state $\bar{\alpha}$ plus a sum of terms representing incoming spherical waves. Thus only the ionic term $\bar{\alpha}$ has an outgoing wave. One uses the wavefunction in (10) to calculate the angular distribution of photoelectrons.

## The Photoionization Cross Section

If one writes the interaction Hamiltonian in (4) as $H_{int}(t) = H_{int}(0)^{-i\omega t}$, then standard procedures of first order time-dependent perturbation theory show that the transition rate for transition from an initial atomic state with energy $E_0$ and wavefunction $\psi_0$ to a final state described by the wavefunction $\psi^-_{\bar{\alpha}\vec{k}_\alpha}$ with total energy $E_f$ is:

$$dW_{\vec{k}_\alpha} = 2\pi \, | < \psi_0 | H_{int}(0) | \psi^-_{\bar{\alpha}\vec{k}_\alpha} > |^2 \delta(E_f - E_0 - \omega) k_\alpha^2 dk_\alpha \, d\Omega(\hat{k}_\alpha) \quad (12)$$

Here the delta function expresses energy conservation and the last factors on the right are the phase space factors for the photoelectron. Dividing the transition rate by the incident photon current density c/V, integrating over $dk_\alpha$, and writing out $H_{int}(0)$ explicitly, we obtain the differential photoionization cross section as

$$\frac{d\sigma_{\bar{\alpha}}}{d\Omega} = \frac{4\pi^2}{c} \frac{k_\alpha}{\omega} \, | \, \hat{\varepsilon} \cdot < \psi_0 | \sum_{i=1}^{N} \vec{p}_i | \psi^-_{\bar{\alpha}\vec{k}_\alpha} > |^2 \quad . \quad (13)$$

Implicit in Eqs. (12) and (13) is an average over initial magnetic quantum numbers $M_{L_0} \; M_{S_0}$ and a sum over final magnetic quantum numbers $M_{\bar{L}} M_{\bar{S}} m_{\bar{s}}$. The length form of Eq. (13) is obtained by replacing each $\vec{p}_i$ by $\omega\vec{r}_i$ (cf. Eq. (6a)).

Substitution of the final state wavefunction (10) in Eq. (13) permits one to carry out the numerous summations over magnetic quantum numbers and obtain the following form for the differential cross section:[8]

$$\frac{d\sigma_{\bar{\alpha}}}{d\Omega} = \frac{\sigma_{\bar{\alpha}}}{4\pi} [1 + \beta \, P_2 \, (\cos \theta)] \quad (14)$$

Here $\sigma_{\bar{\alpha}}$ is the partial cross section for leaving the ion in the state $\bar{\alpha}$, $\beta$ is the asymmetry parameter, $P_2(\cos\theta) = \frac{3}{2} \cos^2\theta - \frac{1}{2}$, and $\theta$ indicates the direction of the outgoing photoelectron with respect to the polarization vector $\hat{\varepsilon}$ of the incident light. The form of (14) follows in the electric dipole approximation from general symmetry principles provided that the target atom is unpolarized.[9] The partial cross section is given in terms of reduced electric dipole matrix elements involving the theoretical channel functions in (9a) as follows:

$$\sigma_{\bar{\alpha}} = \frac{4\pi^2}{3c} \, \omega \, [L_0]^{-1} \sum_{\ell_\alpha L} | < \psi_0 \| \sum_{i=1}^{N} r_i [1] \| \psi^-_{\alpha E} > |^2 \quad (15)$$

The $\beta$ parameter has a much more complicated expression involving interference between different reduced dipole amplitudes. Thus measurement of $\beta$ provides information on the relative phases of the alternative final state channel wavefunctions, whereas the partial cross-section in Eq. (15) obviously does not. From the

requirement that the differential cross section in (14) be positive, one easily sees that $-1 \leq \beta \leq +2$.

The cross section and angular distribution asymmetry parameter $\beta$ thus depend on the reduced dipole amplitudes shown in (15). In most theoretical formulations, both $\psi_0$ and $\psi_{\alpha E}$ are represented in terms of a basis of single particle radial wavefunctions. Thus, the dynamical part of the reduced matrix elements is represented by the one-electron radial matrix element of r between initial and final radial wavefunctions. In the next section we examine the behavior of such radial matrix elements within the central potential model.

## CENTRAL POTENTIAL MODEL PREDICTIONS

### Central Potential Model

In the central potential (CP) model the exact atomic Hamiltonian in (1) is approximated by a sum of single-particle terms describing the independent motion of each of the atom's electrons in a central potential V(r):

$$H_{CP} = \sum_{i=1}^{N} \left\{ \frac{p_i^2}{2m} + V(r_i) \right\} \tag{16}$$

The potential V(r) must describe the nuclear attraction and the electron-electron repulsion as well as possible and in particular must satisfy the following boundary conditions at small and large r in the case of a neutral atom:

$$V(r) \xrightarrow[r \to 0]{} \frac{-Z}{r} \quad \text{and} \quad V(r) \xrightarrow[r \to \infty]{} \frac{-1}{r} \tag{17}$$

The Hamiltonian in (16) is separable in spherical coordinates and its eigenstates can be written as Slater determinants of one-electron orbitals of the form $r^{-1}P_{n\ell}\, Y_{\ell m}\,(\Omega)$ for bound orbitals and of the form $r^{-1}\, P_{\varepsilon\ell}(r)\, Y_{\ell m}(\Omega)$ for continuum orbitals. The one-electron radial wave functions are obtained as solutions of

$$\frac{d^2P_{\varepsilon\ell}(r)}{dr^2} + 2\left[\varepsilon - V(r) - \frac{\ell(\ell+1)}{2r^2}\right] P_{\varepsilon\ell}(r) = 0 \tag{18}$$

A similar equation holds for discrete orbitals $P_{n\ell}(r)$. All of the radial wave functions satisfy the boundary condition $P_{\varepsilon\ell}(0) = 0$.

## High Energy Behavior of the Photoionization Cross Section

The hydrogen atom cross section, which is non-zero at threshold and decreases monotonically with increasing photon energy, serves as a model for inner-shell photoionization cross sections in the x-ray photon energy range. Motivation for a hydrogenic treatment at high energies stems from the fact that sharp onsets at threshold followed by monotonic decreases above threshold are precisely the behavior seen in x-ray photoabsorption measurements. A simple hydrogenic approximation at high energies may be justified theoretically as follows: (1) Since a free electron cannot be photoionized due to kinematical considerations, at high photon energies one expects the more strongly bound inner electrons to be preferentially ionized as compared to the outer electrons. (2) Since the wave function $P_{n\ell}(r)$ for an inner electron is concentrated in a very small range of r one expects the integrand of the radial dipole matrix element to be negligible except for those r where $P_{n\ell}(r)$ is greatest. (3) Thus it is only necessary to approximate the atomic potential locally, e.g., by means of a screened Coulomb potential appropriate for the $n\ell^{\underline{th}}$ orbital:

$$V_{n\ell}(r) = -\left(\frac{Z - s_{n\ell}}{r}\right) + V_{n\ell}^{o} \quad . \tag{19}$$

Here $s_{n\ell}$ is the "inner-screening" parameter, which accounts for the screening of the nuclear charge by the other atomic electrons, and $V_{n\ell}^{o}$ is the "outer-screening" parameter, which accounts for the lowering of the $n\ell$ electrons' binding energy due to repulsion between the outer electrons and the photoelectron as the latter leaves the atom. The potential in (19) predicts hydrogen-like photoionization cross sections for inner-shell electrons with onsets determined by the outer-screening parameters $V_{n\ell}^{o}$. These predictions of the simple hydrogenic model are clearly confirmed by the more accurate numerical calculations of Botto et al.[10] for the K-shell photoionization cross sections of Fe, $Fe^{+16}$, $Fe^{+18}$, $Fe^{+20}$, and $Fe^{+23}$ shown in Fig. 1. One sees that changes in the outer screening only affect the binding energy of the 1s electron and hence the onset of photoionization. The value of the photoionization cross section at a given photon energy $\omega$ is nearly independent of changes in $V_{n\ell}^{o}$, as predicted by Eq. (19).

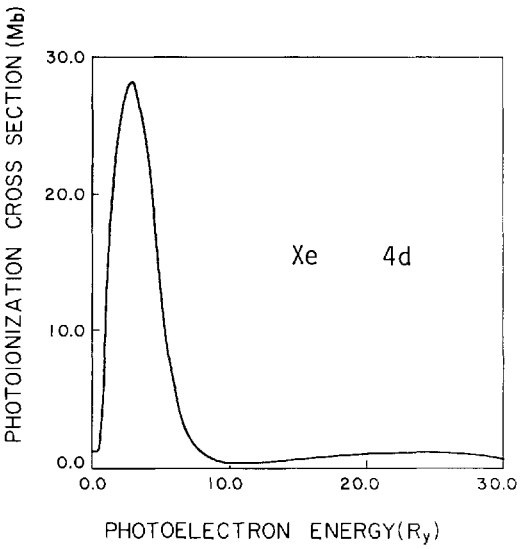


Fig. 2. Theoretical photoionization cross section for the 4d subshell in Xe vs. photoelectron energy. (Hartree-Fock length results from Ref. 16).

threshold). Then it decreases to a minimum (the so-called Cooper minimum[17,18]) and rises to a second maximum. Finally the cross section decreases monotonically at high energies in accordance with hydrogenic behavior. The non-hydrogenic behavior in Fig. 2 may be interpreted as due either to an effective potential barrier or to a zero in the radial dipole matrix element. We examine each of these effects in turn.

Potential Barrier Effects. The excited electron wavefunction obeys the radial equation (18), which contains the effective potential

$$V_{eff}(r) \equiv V(r) + \frac{\ell(\ell+1)}{2r^2} \quad . \tag{21}$$

When $V(r)$ is a Coulomb potential, $V_{eff}(r)$ is always a single well potential having a repulsive barrier near $r = 0$ and an attractive long-range Coulomb tail. Realistic atomic potentials $V(r)$, however, are quite non-Coulombic for values of $r$ near the radii of outer atomic subshells. In many cases for $\ell \geq 2$, $V_{eff}(r)$ becomes positive

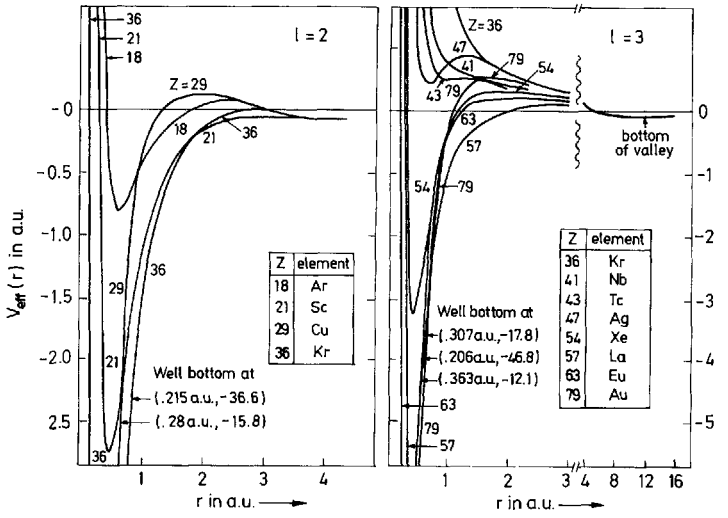


Fig. 3. Effective potential $V_{eff}(r)$ vs. coordinate r for $\ell = 2$ and $\ell = 3$ electrons. (From Ref. 20).

at these radii resulting in a two-well potential, i.e., $V_{eff}(r)$ has a potential barrier at intermediate values of r.[19] Fig. 3 shows $V_{eff}(r)$ for $\ell = 2$ and $\ell = 3$ calculated[20] using the Herman-Skillman[21] atomic potentials V(r). Note in particular that for $\ell = 3$ xenon (Z = 54) has a potential barrier for $1 \leq r \leq 4$ a.u. If we note that the 4d-subshell cross section in Fig. 2 results primarily from the $4d \rightarrow \varepsilon f$ one-electron transition, then the potential barrier for $\ell = 3$ explains the delayed onset of the cross section maximum.

Consideration of the xenon 4d and εf wavefunctions calculated according to Eq. (18) shows even more clearly the effect of the $\ell = 3$ potential barrier. One sees in Fig. 4 that at threshold the $\varepsilon = 0.0$ f-wave is kept out of the inner well region by the potential barrier so that there is hardly any overlap with the bound 4d orbital. Only for a kinetic energy $\varepsilon = 0.3$ a.u. above the barrier can the continuum wavefunction move in toward smaller r, resulting in a large overlap with the 4d wavefunction and hence a cross section maximum.

Effects of zeros in the dipole matrix element. The existence of a minimum in the cross section for photoionization of the outer

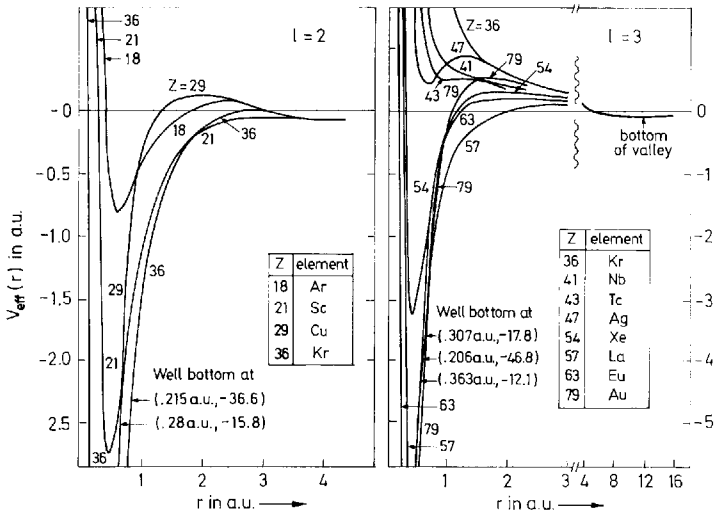


Fig. 3. Effective potential $V_{eff}(r)$ vs. coordinate r for $\ell = 2$ and $\ell = 3$ electrons. (From Ref. 20).

at these radii resulting in a two-well potential, i.e., $V_{eff}(r)$ has a potential barrier at intermediate values of r.[19] Fig. 3 shows $V_{eff}(r)$ for $\ell = 2$ and $\ell = 3$ calculated[20] using the Herman-Skillman[21] atomic potentials V(r). Note in particular that for $\ell = 3$ xenon (Z = 54) has a potential barrier for $1 \leq r \leq 4$ a.u. If we note that the 4d-subshell cross section in Fig. 2 results primarily from the $4d \rightarrow \varepsilon f$ one-electron transition, then the potential barrier for $\ell = 3$ explains the delayed onset of the cross section maximum.

Consideration of the xenon 4d and εf wavefunctions calculated according to Eq. (18) shows even more clearly the effect of the $\ell = 3$ potential barrier. One sees in Fig. 4 that at threshold the $\varepsilon = 0.0$ f-wave is kept out of the inner well region by the potential barrier so that there is hardly any overlap with the bound 4d orbital. Only for a kinetic energy $\varepsilon = 0.3$ a.u. above the barrier can the continuum wavefunction move in toward smaller r, resulting in a large overlap with the 4d wavefunction and hence a cross section maximum.

Effects of zeros in the dipole matrix element. The existence of a minimum in the cross section for photoionization of the outer

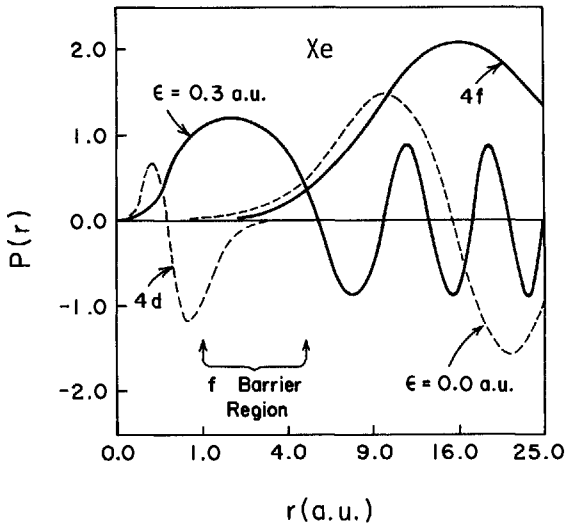


Fig. 4. Xenon $\ell$=3 orbitals; 4f (energy normalized), $\varepsilon$ = 0.0 a.u., and $\varepsilon$ = 0.3 a.u. radial wavefunctions computed using the Herman-Skillman atomic potential. The xenon 4d orbital, normalized to unity, is also shown.

s electron in the alkalis has long been known to be due to a change in sign of the dipole integral with increasing photoelectron kinetic energy.[22,23] Cooper[17] and Fano and Cooper[18] formulated the following general rule for the occurrence of such sign changes: *The radial dipole matrix element for the transition* $n\ell \rightarrow n'\ell'$ *(where* $n'$ *extends over all discrete excited states* $n' > n$ *as well as the continuum) will change sign as a function of* $n'$ *when* $\ell'$ *states with* $n' = n$ *exist but are not occupied in the ground state of the atom.* Note that this rule excludes $n\ell$ = 1s, 2p, 3d, and 4f, all of which have positive (nodeless) radial wavefunctions, as well as the transitions $n\ell \rightarrow n'\ell-1$, which are always weaker than $n\ell \rightarrow n'\ell+1$. The rule amounts in principle to a prediction of the occurrence of a negative radial dipole integral for low-energy final-state wavefunctions. The physical basis for this rule comes partly from known results for atomic hydrogen and partly from calculational evidence based on the central potential model. Thus, it is known that for hydrogen wavefunctions the radial dipole matrix element is always positive except when $n' = n$.[18] Furthermore, at high energies the radial dipole integral becomes hydrogenic and hence positive. On the other hand, central potential model calculations for atomic ground states show that the radial dipole matrix element for a particular

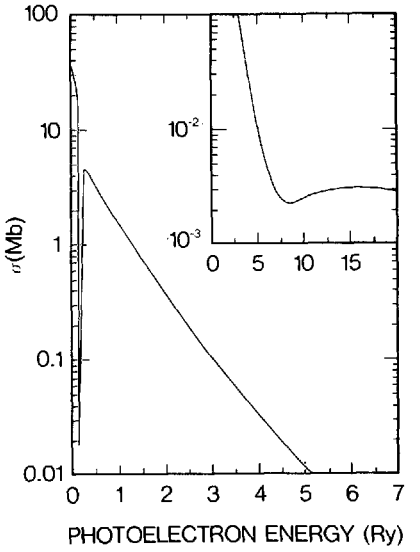


Fig. 5. Photoionization cross section for the excited 5d orbital of Cs. Inset shows the high-energy behavior of the cross section (From Ref. 24).

transition changes sign either once or not at all. Putting these three facts together, one observes that "Cooper minima" will occur for those transitions having a negative radial dipole matrix element at threshold.

The minimum at $\varepsilon \approx 10$ Ry in the Xe 4d-subshell photoionization cross section shown in Fig. 2 may thus be interpreted as due to a sign change in the radial dipole matrix element for the transition $4d \rightarrow \varepsilon f$. As shown in Fig. 4, the overlap of the 4d wavefunction and the final f-wavefunction is negative at the threshold energy $\varepsilon = 0.0$ a.u. At $\varepsilon = 0.3$ a.u. one observes cancellation between positive and negative components of this overlap. At higher $\varepsilon$ the f-wave moves in further toward lower r increasing the cancellation until the radial matrix element passes through zero and becomes positive.

The above rules no longer hold for photoionization from excited-state orbitals, which are very diffuse. Fig. 5 shows the cross section for photoionization of the excited 5d orbital in Cs.[24] The gross shape of the cross section is due to the $5d \rightarrow \varepsilon f$ transition, whose radial dipole matrix element is positive at threshold and

undergoes two changes in sign as $\varepsilon$ increases in energy, one at $\varepsilon \approx 0.17$ Ry and another at $\varepsilon \approx 7.0$ Ry shown in the inset. It was further found that the radial dipole integral for the weak transition $5d \rightarrow \varepsilon p$ also has a zero near $\varepsilon \approx 0.07$ Ry, although this minimum is not noticeable on the scale used in Fig. 5. Fig. 5 illustrates the utility of a central potential model calculation for distinguishing between cross section minima and window resonance features.

Recently, several new theoretical studies on the systematics of cross section minima have been carried out. Kim et al.[25] have shown that in relativistic central potential model calculations the minima occur at much higher energies than in non-relativistic calculations. Furthermore the energy difference between the minima in channels differing only by fine-structure quantum numbers is an order of magnitude greater than the fine structure splitting of the ionic energy levels.[25] In another study, Kim et al.[26] have identified excited states in high Z elements in which the cross section minimum moves in toward threshold in the region of the delayed maximum above threshold. The cross section thus has two maxima of comparable height. Lastly, Msezane and Manson[27] have shown that, in photoionization of excited states, cross section minima occur when the phase shift difference between the initial and final states is about $\pi$ degrees. This may be understood by recalling that in atomic hydrogen there are no cross section minima. The excited states of other atoms, however, are essentially hydrogenic except for a phase shift due to the non-Coulombic ionic core. (The initial discrete orbital "phase shift" is taken to be the quantum defect multiplied by $\pi$, in accordance with quantum defect theory.[28]) When the initial and final states have a phase difference of $\pi$, then, they are out-of-phase with each other relative to the hydrogenic case and hence the radial dipole matrix element is zero.

The importance of cross section minima to theory is often that within such minima one can observe effects of weak interactions that are otherwise obscured. Relativistic and weak correlation effects on the photoelectron angular distribution asymmetry parameter $\beta$ for s-subshells is a notable example that has been discussed in detail elsewhere.[29] Wang et al.[30] have also emphasized that in such minima in the electric dipole amplitudes one cannot ignore the effects of quadrupole and higher corrections to the photoelectron's differential cross section. Central potential model calculations[30] show that quadrupole corrections can be as large as 10% of the electric dipole cross section in such cross section minima even for low photon energies.

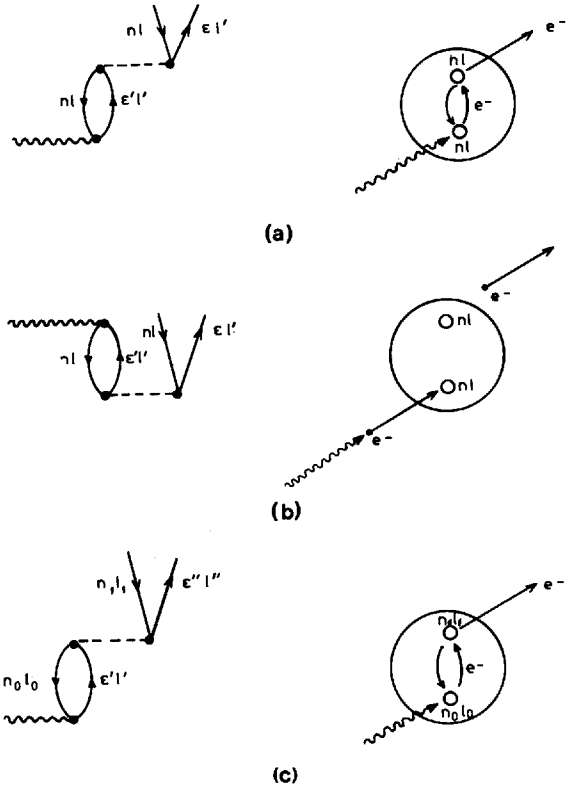


Fig. 6. MBPT diagrams (left) and scattering pictures (right) for three kinds of particle-hole interaction: (a) intrachannel scattering following photoabsorption; (b) photoabsorption by a virtual doubly-excited state; (c) interchannel scattering following photoabsorption.

## THE PARTICLE-HOLE INTERACTIONS

A large number of calculations of the single-photoionization cross section of closed-shell atoms using alternative theoretical formulations have shown that of the many kinds of electron correlation it is the particle-hole interactions which are most important for photoionization. They may be described as interactions in which two electrons either excite or de-excite each other out of or into their initial subshell locations in the unexcited atom. (When an electron is excited out of a subshell it is said to leave

behind a vacancy or hole.) To analyze the effects of these interactions on the cross sections it is convenient to classify them in three categories: intrachannel, virtual double excitation, and interchannel. These alternative kinds of particle-hole interactions are illustrated in Fig. 6 using both many-body perturbation theory (MBPT) diagrams and more "physical" scattering pictures. We discuss each of these types of interaction in turn.

Intrachannel Interactions

The many-body perturbation theory (MBPT) diagram for this interaction is shown on the left in Fig. 6(a); on the right a slightly more pictorial description of this interaction is shown. The wiggly line indicates a photon, which is absorbed by the atom in such a way that an electron is excited out of the $n\ell^{th}$ subshell. During the escape of this excited electron, however, it collides or interacts with another electron from the same subshell in such a way that the second electron absorbs all the energy imparted to the atom by the photon; the first electron is de-excited back to its original location in the $n\ell^{th}$ subshell. For closed-shell atoms, the photoionization process leads to a $^1P_1$ final state in which the intrachannel interaction is strongly repulsive. Hence with respect to central potential model or average-of-configuration Hartree-Fock (HF) calculations, which include only a weaker average intrachannel interaction in generating the basis wave functions, inclusion of these interactions serves to shift the delayed maximum in the cross section to higher energies (usually too high) as well as to broaden this peak and decrease its amplitude. [Note that in those HF calculations (known as term-dependent HF calculations) that include the correct $^1P_1$ intrachannel interaction in solving for the HF wavefunctions no further treatment of these interactions is necessary: one obtains cross sections equivalent to those obtained by starting from an arbitrary basis set of final state wave functions and explicitly treating the intrachannel interactions within this basis set.]

As an example of the effect of intrachannel interactions, consider the 3p-subshell photoionization cross section in Ar shown in Fig. 7. The central-potential model calculation[31] (HS) has the same qualitative features as the experimental data[32] (open circles) but has a cross section that peaks at too low an energy and is far too high and narrow. The solid lines indicate the result of treating the intrachannel interactions within the basis of the central-potential model wave functions.[31] The result using the length form of the dipole matrix element peaks at too high an energy due to the too repulsive intrachannel interaction. The result using the velocity form of the dipole matrix element gives too low a cross

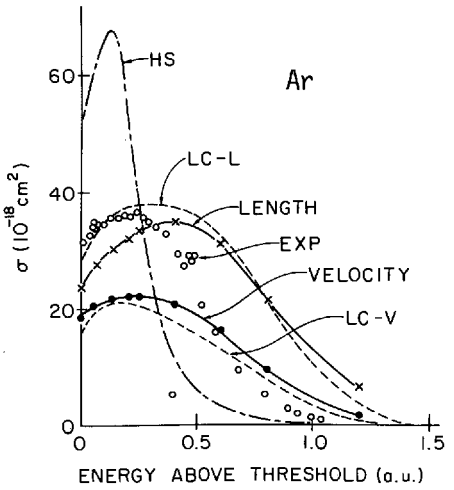


Fig. 7. Photoionization cross sections for the 3p subshell of Ar, -•-, Herman-Skillman central potential model calculation; ——, intrachannel calculation of Starace[31]; ---, close coupling calculation of Lipsky and Cooper; o, experimental results of Samson.[32] (From Ref. 31).

section, again due to the too repulsive intrachannel interaction that keeps the continuum wave function out of the small r region, which is weighted more strongly by the velocity dipole operator. The dashed curves represent close coupling calculations,[33] which include not only the intrachannel interactions but also certain weak interchannel interactions (discussed below) involving the 3s subshell. Clearly the results are not very different from the intrachannel calculations,[31] indicating another cause for the discrepancy with experiment.

Virtual Double Excitations

The MBPT diagram for this type of interaction is shown on the left in Fig. 6(b). Topologically this diagram is similar to that on the left in Fig. 6(a). In fact, the radial parts of the two matrix elements are identical; only the angular factors differ. A more pictorial description of this interaction is shown on the right of Fig. 6(b). The ground state of the atom before photoabsorption is shown to have two electrons virtually excited out of the $n\ell^{\underline{th}}$ subshell. In absorbing the photon, one of these electrons

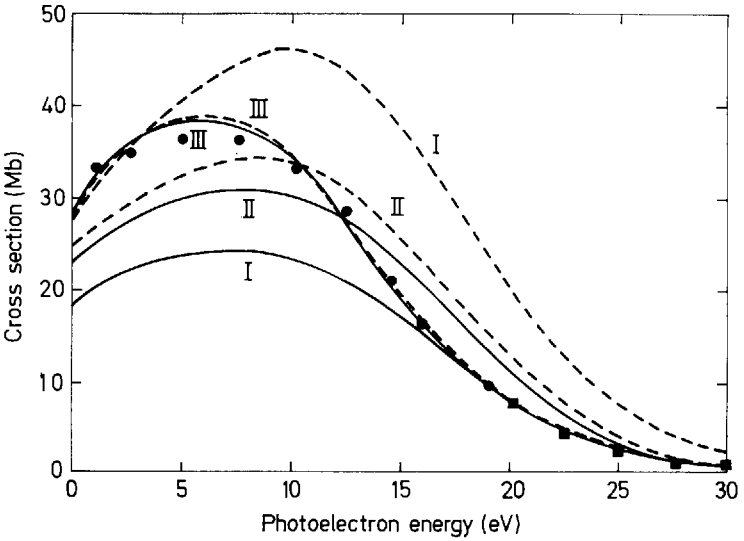


Fig. 8. Theoretical calculations of Chang[34] for the photoionization cross section of the 3p subshell of Ar. Dashed and solid lines give length and velocity results, respectively, in three levels of approximation discussed in the text. Experimentally measured values of the Ar cross section are indicated by the solid circles[32] and by the solid squares (Samson, unpublished). (From Ref. 34).

is de-excited to its original location in the $n\ell^{\underline{th}}$ subshell, while the other electron is ionized. These virtual double excitations imply a more diffuse atom than in central-potential or HF models with the effect that the overly repulsive intrachannel interactions are weakened, leading to cross sections that are in very good agreement with experiment. Recent calculations of Chang[34] for the Ar 3p-subshell cross section (Fig. 8) demonstrate the effect of including these virtual double excitations. The curves labeled I are the length and velocity results including only the intrachannel interactions. Curves II indicate the effect of including virtual double excitations in the initial state: the length and velocity curves are in better agreement, but there is still a sizable discrepancy with the experimental results[32] (solid circles). Finally curves III indicate the result of including virtual double excitations in both the initial and the ionic state. Now the length and velocity curves are virtually identical and are both in excellent agreement with experiment.

## Interchannel Interactions

A last type of particle-hole interaction that has been found to be important, particularly for s subshells, is the interchannel

interaction shown in Fig. 6(c). This interaction has the same form as the intrachannel interaction shown in Fig. 6(a), except now when an electron is photoexcited out of the $n_0\ell_0\underline{^{th}}$ subshell, it collides or interacts with an electron in a different subshell — the $n_1\ell_1\underline{^{th}}$ subshell — in such a way that the second electron is ionized, and the first electron falls back into its original location in the $n_0\ell_0\underline{^{th}}$ subshell. There are two major effects of this interaction: (1) when the binding energy of the $n_0\ell_0\underline{^{th}}$ subshell is greater than that of the $n_1\ell_1\underline{^{th}}$ subshell, discrete members of the $n_0\ell_0\underline{^{th}}$ subshell channels show up as resonances in the $n_1\ell_1$ subshell cross section; (2) when the dipole amplitude for ionization of the $n_1\ell_1\underline{^{th}}$ subshell is small compared with that for the $n_0\ell_0\underline{^{th}}$, for example, when $n_1\ell_1$ is an s subshell, the zero-order $n_1\ell_1\underline{^{th}}$ subshell cross section can be strongly modified by interchannel interactions.

As an example of the first effect — resonance behavior — we consider once again the photoionization of the 3p subshell in Ar, this time including also the effect of interchannel interaction with the 3s subshell. The channels under consideration are thus

$$\begin{aligned} Ar3s^2 3p^6 + \gamma &\rightarrow Ar^+ 3s^2 3p^5 + e^- \\ &\rightarrow Ar^+ 3s3p^6 + e^- \ . \end{aligned} \tag{22}$$

Figure 9 shows the MBPT calculation of Kelly and Simons,[35] which includes both intrachannel and interchannel interactions as well as the effect of virtual double excitations. The cross section is in excellent agreement with experiment,[32,36] even to the extent of describing the resonance behavior due to discrete members of the $3s \rightarrow \varepsilon p$ channel.

As an example of the second effect, strong modification of a weak dipole amplitude, we consider again the two channels in Eq. (22), but this time we focus on the 3s-subshell cross section. Figure 10 shows three calculations, which include intrachannel and interchannel interactions as well as virtual double excitations. There are the R-matrix calculation of Burke and Taylor,[37] the random phase approximation (RPA) calculation of Amusia et al.,[38] and the simplified RPA calculation of Lin.[39] As compared with the HF calculation[16] shown, which only includes the intrachannel interactions, these three other calculations show that interchannel interactions introduce a strong interference between the channels in Eq. (22). This interference causes a minimum in the 3s-subshell cross section in agreement with experiment.[40,41]

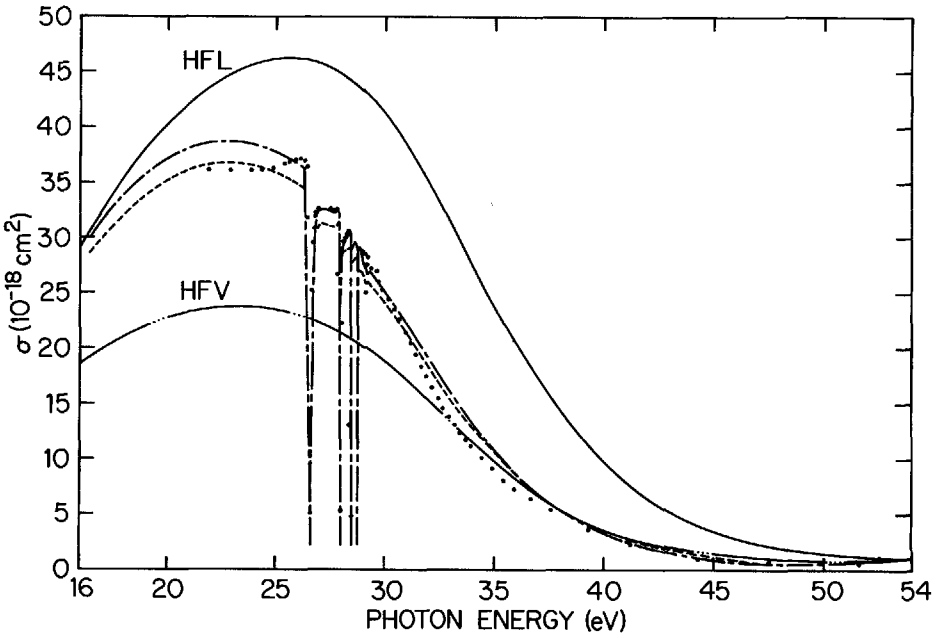


Fig. 9. Photoionization cross section for the 3p and 3s subshells of Ar. HFL and HFV indicate the length and velocity results obtained using HF orbitals calculated in a $^1P_1$ potential. Dot-dash and dashed lines represent the length and velocity results of the MBPT calculation of Kelly and Simons.[35] Only the four lowest $3s \rightarrow np$ resonances are shown; the series converges to the 3s threshold at 29.24 eV. Experimental results are those of Samson[32] above 37 eV and of Madden et al.[36] below 37 eV. (From Ref. 35).

As a final example of particularly strong interchannel interactions we consider the 5s-subshell cross section in Xe as influenced by the neighboring 4d and 5p subshells. The relevant channels are

$$\begin{aligned} Xe4d^{10}5s^25p^6 + \gamma &\rightarrow Xe^+4d^95s^25p^6 + e^- \\ &\rightarrow Xe^+4d^{10}5s5p^6 + e^- \\ &\rightarrow Xe^+4d^{10}5s^25p^5 + e^- \ . \end{aligned} \tag{23}$$

Figure 11 shows the calculations of Amusia and Cherepkov[7] in three approximations. The dot-dash line represents the HF result for the 5s-subshell cross section. No interchannel interactions are included. The dashed line represents an RPA calculation including interchannel interaction with the $4d \rightarrow \varepsilon f$ channel. One sees that

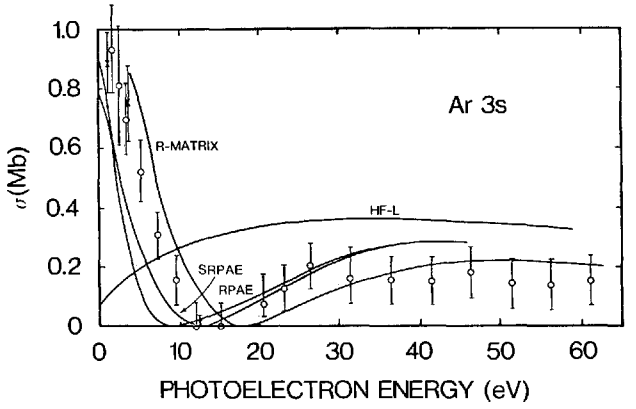


Fig. 10. Photoionization cross section for the 3s subshell of Ar: R-matrix, R-matrix (length) calculation of Burke and Taylor[37]; RPAE, RPA calculation of Amusia et al.[38]; SRPAE, simplified RPA calculation of Lin[39]; HF-L, Hartree-Fock (length) calculation of Kennedy and Manson[16]; ×, experimental data of Samson and Gardner[40]; ○, experimental data of Houlgate et al.[41] (From Houlgate et al.[41]).

the large delayed maximum in the 4d-subshell cross section (compare Fig. 2) is mirrored in the 5s-subshell cross section. The solid line represents an RPA calculation including interchannel interaction with both the $4d \to \varepsilon f$ and the $5p \to \varepsilon d$ channels. One sees that interchannel interaction with the outer 5p subshell produces interference leading to a zero in the 5s-subshell cross section.

Remarks

The three types of interactions discussed are the most important for the outer $\ell \geq 1$ subshells of the rare gases and probably for all closed-shell atoms. These interactions form the essential physical content of the many ab initio theoretical methods that have been developed to treat atomic photoionization such as the RPA,[7,42] the MBPT,[43] R-matrix method,[37,44] the transition matrix

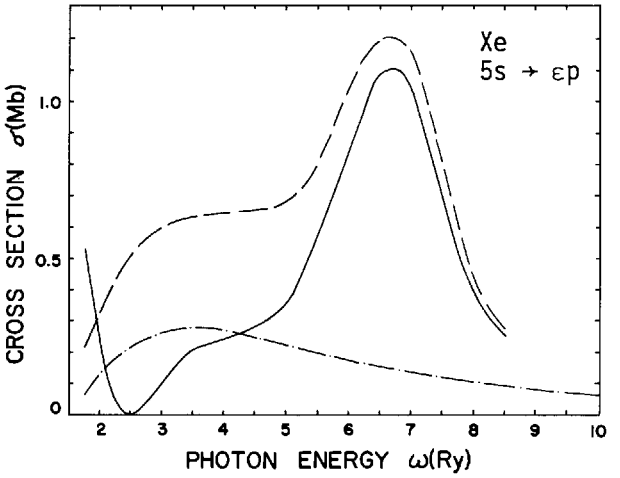


Fig. 11. Theoretical calculations of Amusia and Cherepkov[7] for the photoionization cross section of the 5s subshell of Xe, showing the influence of interchannel interactions (see text for deacription of curves) (From Ref. 7).

approach,[34,45] and the multiconfiguration HF approach[46] among others. We emphasize, however, that except for the RPA these methods are not restricted to treating only the particle-hole class of interactions. In particular, s subshells have such small cross sections that other types of interaction may have a significant influence on them.[7] Table 1 indicates the interactions taken into account in the major approximation methods developed for atomic photoionization. Note that in taking all particle-hole interactions into account to infinite order the RPA opts for simplicity at the expense of a certain amount of violation of the Pauli Principle in higher orders of perturbation. Errors in the photoionization cross section due to these violations have been estimated to be less than 10%.[7] The fact that both the MBPT and the RPA achieve comparable agreement with experiment indicates that higher order terms in interchannel interaction and in virtual double excitations are not very important, at least for closed shell atoms.

Among those additional interactions that are important in closed-shell atom photoionization, relativistic interactions stand out since experimentalists can resolve fine structure as well as obtain photoelectron spin polarizations, both of which require a

Table 1: Comparison of Major Theoretical Methods for Atomic Photoionization

| | Method | Intrachannel Interactions | Interchannel Interactions | Virtual Double Excitations |
|---|---|---|---|---|
| (1) | Central Potential Model | Not treated | Not treated | Not treated |
| (2) | Term-Dependent Hartree-Fock | ∞ Order | Not treated | Not treated |
| (3) | MBPT | ∞ Order | Usually to 1st or 2nd Order | Usually to 1st or 2nd Order |
| (4) | Close-Coupling and R-Matrix Methods | ∞ Order | ∞ Order | Treated By Configuration Interaction |
| (5) | RPA | ∞ Order | ∞ Order | ∞ Order Pauli Principle Violated in 2nd and higher orders |

relativistic treatment for their theoretical description. Furthermore when cross sections are small, relativistic effects can stand out in a striking way. The relativistic RPA theory of Johnson and co-workers[47-49] includes not only the particle-hole interactions described above but also relativistic interactions. It thus represents the state-of-the-art for the theoretical description of photoionization processes involving closed-shell atoms. Results for partial cross sections,[48] fine-structure branching ratios,[48] photoelectron angular distributions,[48] and photoelectron spin polarizations[49] are all in excellent agreement with experiment.

Except for the lightest atoms, relatively few open-shell atoms have been studied in detail either experimentally or theoretically. On the one hand this is due to the experimental difficulty of producing open-shell atom vapors and on the other hand to the greater number of channels that must be considered in a theoretical calculation. For this reason one can only speculate whether or not open-shell atom cross sections will require theoreticians to treat any interactions in addition to the particle-hole interactions in

order to obtain good agreement with experiment. Of the theoretical methods developed to describe closed-shell atom photoionization processes, the MBPT[43] and R-matrix[37,44] method are not restricted to closed-shell atoms. Recently both the RPA[50] and the transition matrix method[51] have been generalized to treat open-shell atoms. What is now required are many detailed experimental measurements to test the various theoretical methods as well as our understanding of the electron correlations involved.

## HYPERSPHERICAL COORDINATE DESCRIPTION OF PHOTOIONIZATION

So far we have focused on photoionization processes in which only a single electron is photoionized and the ion is left in a stationary state. Increasingly, however, interest has focused on photoionization processes in which two electrons move outside an ionic core such as in double photoionization, in photoionization plus excitation, and in post-collision interaction and other relaxation processes in which a second electron is ionized or excited. (These latter relaxation processes are often considered as distinct from double photoionization or photoionization plus excitation only because the two electrons usually come from different subshells.) Knowledge of the electron dynamics when both electrons share comparable amounts of energy near the nucleus is crucial to understanding the excitation process. For this reason we focus in this section on the hyperspherical coordinate formulation of atomic photoionization since it treats the motion of two electrons outside an ionic core on an equal footing. Within a separable approximation the method has provided a new classification of whole series doubly excited states. Furthermore the separable approximation has proved to be a quantitatively accurate first approximation to two-electron level energies and single-electron photoionization cross sections. Analysis of the breakdown of separability has provided new insight into the photoexcitation process and quantitative treatments of such processes are being developed.

### Two-Electron Schrödinger Equation in Hyperspherical Coordinates

The hyperspherical coordinate system for two electrons outside of a massive center is defined by introducing the mean square radius of the two electrons from the nucleus,

$$R = (r_1^2 + r_2^2)^{1/2} \tag{24a}$$

and a corresponding angular coordinate

$$\tan \alpha = r_2/r_1 \tag{24b}$$

The radius R measures the "size" of the two electron state, while the angle $\alpha$ measures the radial correlation of the two electrons. Note that when $\alpha = \pi/4$, $r_1 = r_2$; when $\alpha = 0$ or $\pi/2$, one of the electrons is at a much larger distance from the nucleus than the other.

In this system of coordinates the non-relativistic two-electron Schrödinger equation becomes

$$\left\{ \frac{d^2}{dR^2} - \left[ \frac{1}{R^2} \left( - \frac{d^2}{d\alpha^2} - \frac{1}{4} + \frac{\ell_1^2}{\cos^2\alpha} + \frac{\ell_2^2}{\sin^2\alpha} \right) - \frac{C(\alpha,\theta_{12})}{R} \right] + 2E \right\} \times (R^{5/2} \sin\alpha \cos\alpha \Psi) = 0 \tag{25}$$

where

$$-C(\alpha,\theta_{12}) = R \left( - \frac{2Z}{r_1} - \frac{2Z}{r_2} + \frac{2}{|\vec{r}_2 - \vec{r}_1|} \right) = - \frac{2Z}{\cos\alpha} - \frac{2Z}{\sin\alpha} + \frac{2}{(1 - \sin 2\alpha \cos\theta_{12})^{1/2}} \tag{26}$$

and $\vec{\ell}_1$ and $\vec{\ell}_2$ are the usual orbital angular momentum operators for the individual electrons, $\theta_{12} \equiv \cos^{-1} \hat{r}_1 \cdot \hat{r}_2$, and Z is the nuclear charge.

In the hyperspherical coordinate method of Macek,[52] the two electron wavefunction $\psi_\nu(\vec{r}_1,\vec{r}_2)$ is expanded in terms of a complete set of adiabatic eigenfunctions $\phi_\mu(R;\alpha,\hat{r}_1,\hat{r}_2)$, which depend parametrically on the hyperspherical radius $R \equiv (r_1^2 + r_2^2)^{1/2}$ and are functions of the five angular variables $\alpha \equiv \tan^{-1}(r_2/r_1)$, $\hat{r}_1$ and $\hat{r}_2$. The form of $\psi$ is thus:

$$\psi_\nu(R,\alpha,\hat{r}_1,\hat{r}_2) = (R^{5/2} \sin\alpha \cos\alpha)^{-1} \sum_\mu F_{\mu\nu}(R) \phi_\mu(R;\alpha,\hat{r}_1,\hat{r}_2) \tag{27}$$

The angular function $\phi_\mu$ is defined to satisfy the following differential equation in atomic units ($\hbar = e = m = 1$):

$$\left[ -\frac{d^2}{d\alpha^2} + \frac{\ell_1^2}{\cos^2\alpha} + \frac{\ell_2^2}{\sin^2\alpha} - RC(\alpha,\theta_{12}) \right] \phi_\mu = -U_\mu(R)\phi_\mu \ . \qquad (28)$$

Here $-C(\alpha,\theta_{12})$ is defined in Eq. (26) and $U_\nu(R)$ is an eigenvalue which is parametrically dependent on R. Upon substituting equation (27) in the two-electron Schrödinger equation and using equation (28), one obtains the following set of coupled differential equations for the radial functions $F_{\mu\nu}(R)$:

$$\frac{d^2}{dR^2} + \left[ \frac{U_\mu(R) + \frac{1}{4}}{R^2} + \left( \phi_\mu, \frac{\partial^2 \phi_\mu}{\partial R^2} \right) + 2E \right] F_{\mu\nu}(R)$$

$$+ \sum_{\mu' \neq \mu} \left[ \left( \phi_\mu, \frac{\partial^2 \phi_{\mu'}}{\partial R^2} \right) + 2 \left( \phi_\mu, \frac{\partial \phi_{\mu'}}{\partial R} \right) \frac{\partial}{\partial R} \right] F_{\mu'\nu}(R) = 0. \qquad (29)$$

In equation (29) the coupling matrix elements $(\phi_\mu, \partial^n \phi_{\mu'}/\partial R^n)$, n = 1,2, involve integration over the five angular variables only and are thus parametrically dependent on R.

The Separable Approximation

Each of the potentials $U_\mu(R)$ and its corresponding angular eigenfunction $\phi_\mu$ define a hyperspherical channel $\mu$. These channels are coupled through the radial derivative matrix elements in Eq. (29). In a separable — or adiabatic — approximation,[52] one ignores the coupling terms in the second set of braces in Eq. (29). Then the wavefunction in Eq. (27) may be represented by a single term with $\mu = \nu$ in the summation on the right hand side, i.e.,

$$\psi_{\mu E}^{\text{Sep.}} = (R^{5/2} \sin\alpha \cos\alpha)^{-1} F_{\mu\mu E}(R) \phi_\mu(R;\alpha,\hat{r}_1,\hat{r}_2) \ . \qquad (30)$$

For simplicity one usually sets $\mu = \nu$ and drops the double subscripts on F when referring to the separable approximation solutions. One sees from Eq. (30) that the separable approximation amounts to assuming that motion in R and in $\alpha$ are approximately independent of each other. This may be confirmed by examining correlated two-electron wavefunctions and observing that the nodal lines of such wavefunctions lie approximately along constant R and along constant $\alpha$.[53]

The separable approximation has been very successful in classifying and describing the essential properties of Rydberg series of doubly excited states in both helium[52,54] and in the negative ion of hydrogen.[55,56] The index $\mu$ labels the channels. The wavefunction $\psi^{Sep.}_{\mu E}$ for the member of energy E in channel $\mu$ is the product of the angle function $\phi_\mu$ characteristic of the entire channel and the radial function $F_{\mu E}(R)$ obtained by solving the radial Eq. (29) using the channel potential $U_\mu(R)$ and ignoring the off-diagonal coupling terms. Because each member of a Rydberg series of doubly excited states has the same angular function $\phi_\mu$ and has a radial function $F_{\mu E}(R)$ that is calculated in the same potential $U_\mu(R)$, the physical properties of the various channels $\mu$ are often immediately apparent upon examination of $U_\mu(R)$ and $\phi_\mu$. Furthermore, for the lowest energy states calculated in the potentials $U_\mu(R)$, the separable approximation energies and wavefunctions are usually very well determined. Higher energy states of a particular channel $\mu$ calculated in the potential $U_\mu(R)$ are however increasingly too high in energy,[52] if bound, or have too negative phase shifts,[57,58] if unbound.

A recent calculation[58] of the photoionization cross section of He using separable approximation hyperspherical coordinate wavefunctions demonstrates the strengths and weaknesses of this approximation. The initial and final wavefunctions, $\psi_i$ and $\psi_f$, for the process

$$He(^1S) + \gamma \longrightarrow He^+ 1s(^2S) + e^- (^1P) \qquad (31)$$

both have the form of Eq. (30). For the initial state, $\mu$ corresponds to the lowest $^1S$ potential $U_\mu(R)$, and for the final state, $\mu$ corresponds to the lowest $^1P$ potential $U_\mu(R)$. The photoionization cross section obtained using the separable hyperspherical approximation is shown in Fig. 12. Figure 12 also shows the revised experimental data of Samson,[59] which have error bars of ± 3%. The results lie within these error limits near threshold (for kinetic energies $0.0 \leqslant \varepsilon \leqslant 0.4$ au) but are lower than experiment at higher energies. Of the many other theoretical calculations, we show the one with the best overall agreement with experiment: the four-channel (i.e. $1s\text{-}2\bar{s}\text{-}2\bar{p}$) close-coupling calculations of Jacobs.[60] The single-channel hyperspherical calculations do not include coupling to excited states of $He^+$. Unpublished calculations[61] in which the lowest four hyperspherical channels were coupled together show that while the cross sections are improved, they are not better than the four-channel close coupling results at energies

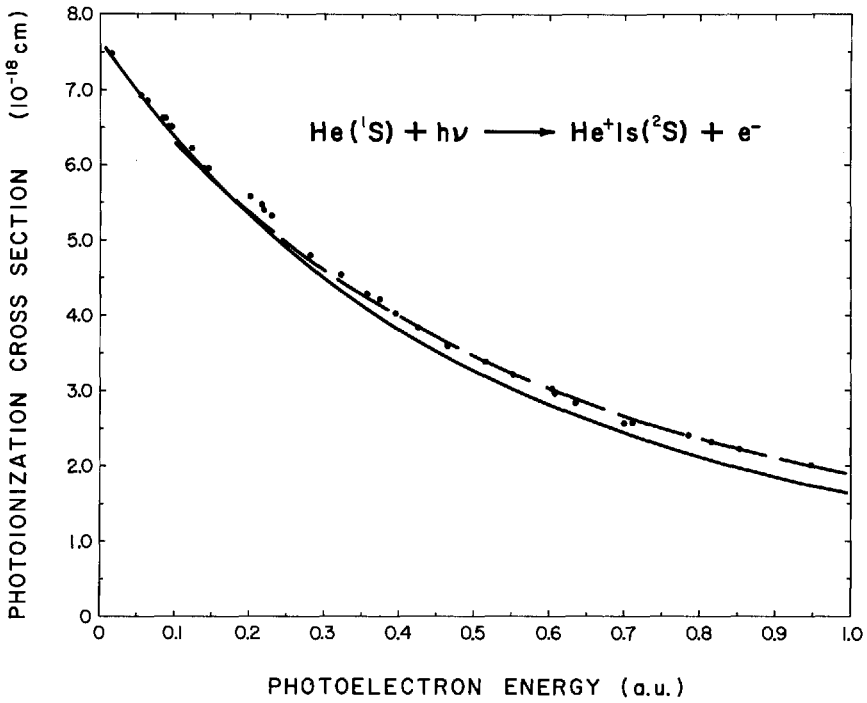


Fig. 12. Photoionization cross section for He. Full curve, separable approximation (single-channel) hyperspherical calculation of Miller and Starace (Ref. 58); dots, experimental measurements of Samson (Ref. 59); dashed curve, $1s - 2\bar{s} - 2\bar{p}$ (four-channel) close-coupling calculation of Jacobs (Ref. 60).

$\varepsilon \gtrsim 0.2$ a.u. Thus one has the peculiar situation where for energies $\varepsilon \lesssim 0.2$ a.u. above the ionization threshold the single-channel separable approximation hyperspherical calculations agree to within 1% with experiment and are as good as or better than a four-channel close-coupling calculation; but for energies $\varepsilon \gtrsim 0.2$ a.u. above threshold the hyperspherical calculations are systematically lower than both experiment and the close-coupling results even when four hyperspherical channels are coupled together. Similar findings have been obtained by Lin[57] for $e^-$ - H scattering phase shifts. We shall discuss a new procedure to overcome this slow convergence of the hyperspherical coordinate method below. Beforehand, however, we wish to show how excitation processes, which involve the breakdown

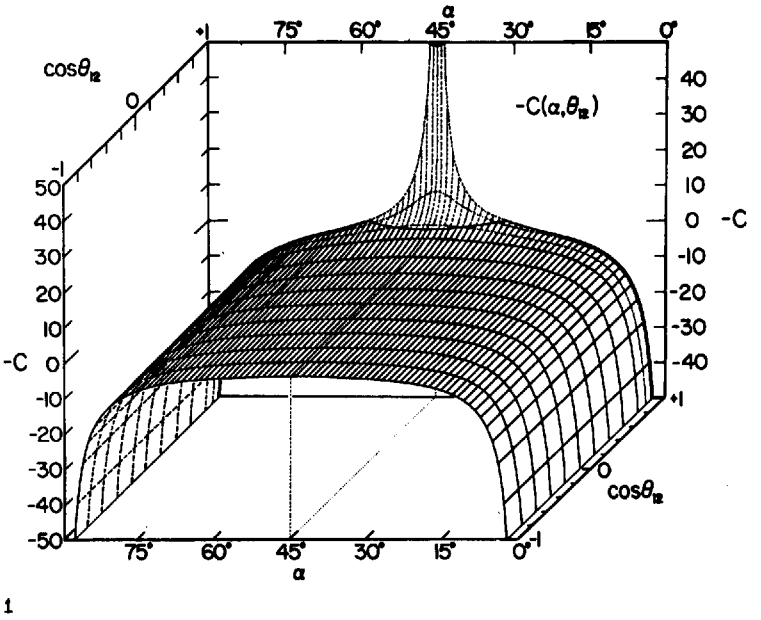


Fig. 13. Relief map of the potential $-C(\alpha,\theta_{12})$ defined in Eq. (26) for Z = 1. (From Ref. 63).

of the separable approximation, are described in the hyperspherical coordinate approach.

Description of Electronic Excitation

The hyperspherical coordinate approach has been used to understand qualitatively how a low-energy two electron state concentrated near the origin, upon receiving energy during a collision process, evolves to states of high excitation far from the origin. The key idea, stressed recently by Fano[62] and illustrated graphically by Lin,[53,63] is that such states describe motion along a potential ridge centered about the direction $\alpha = \pi/4$ (i.e., $r_1 = r_2$).

Consider Eq. (28) for the channel functions $\phi_\mu(R;\alpha,\hat{r}_1,\hat{r}_2)$. The potential $-C(\alpha,\theta_{12})$, defined in Eq. (26), is shown in Fig. 13 for Z=1. States having one electron more excited than the other, i.e., $r_2 >> r_1$ or $r_1 >> r_2$, have an angle function $\phi_\mu$ with maximum amplitude in the valleys of the potential in Fig. 13, near $\alpha = 0$

and $\alpha = \pi/2$. Comparably excited, doubly-excited states have $r_1 \sim r_2$ and thus the angle function $\phi_\mu$ for these states has maximum amplitude on the ridge of the potential in Fig. 13, near $\alpha = \pi/4$, and preferably near $\cos\theta_{12} = -1$ (i.e., on opposite sides of the nucleus). Consider now the R-dependence of the angle functions $\phi_\mu$. Eq. (28) shows that the potential -C is multiplied by R. For large enough R, therefore, the potential -RC on the ridge becomes equal to the eigenvalue $-U_\mu(R)$. At this "classical turning point" the angle function $\phi_\mu$ has no more "kinetic energy" of motion in $\alpha$ on the ridge. For larger R values, its amplitude on the ridge is exponentially damped and the probability amplitude in the channel $\mu$ must retreat to the valleys of the potential in Fig. 13, implying that for such large R values $\mu$ describes states with one electron more highly excited than the other. Alternatively, the two electron state on the ridge may "hop" to the next higher channel $\mu'$. With a higher value of $-U_{\mu'}(R)$, the two electron excitation could move to somewhat larger R along the ridge since the difference between $-U_{\mu'}$ and the top of the potential ridge of -RC would restore some positive "kinetic energy" of motion in $\alpha$. Actually the vicinity of the classical turning point is propitious for such a transition to a higher channel $\mu'$ since the coupling matrix elements (cf. Eq. (29)) are largest precisely where the channel functions are changing most rapidly with R.

Lin[53] has shown graphically how the channel functions $\phi_\mu$ behave as functions of R. Figs. 14 and 15 show the $H^-(^1S)$ channel functions $\phi_\mu(R;\alpha,\theta_{12})$ for $\mu = 1$ and $\mu = 2$ (i.e., the lowest two $^1S$ hyperspherical channels). In Fig. 14 one sees that at R = 1 the charge distribution in the first channel is peaked about $\alpha = \pi/4$, lying on the potential ridge. At R = 4, however, the charge distribution is vacating the ridge and moving to the valleys near $\alpha = 0$ and $\alpha = \pi/2$. By R = 8, $\mu = 1$ describes a channel with one electron much more highly excited than the other. Fig. 15 shows the next higher hyperspherical channel function. Note that at R = 4, precisely where $\mu = 1$ has a depression along the ridge, the $\mu = 2$ channel's charge distribution has a maximum. This peak in $\mu = 2$ along the ridge progresses outward to larger R values until at R = 12 a depression appears along the ridge. If two-electron states in $\mu = 2$ are to move to larger R and remain comparably excited they must hop again to the next higher hyperspherical channel, and so on.

This new perspective of two electron excitation states evolving toward large radii R along a potential ridge has its origins in the Wannier-Peterkop-Rau[64] analysis of electron impact ionization near threshold. Its application to quantitative predictions of excitation cross sections is only just beginning. Of particular interest

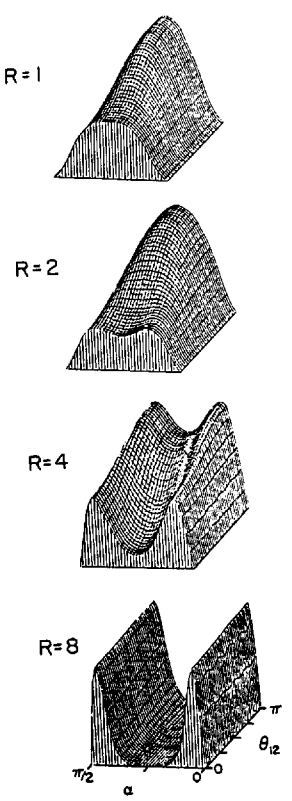


Fig. 14. Plot of $|\phi_\mu(R;\alpha,\theta_{12})|^2$ vs. $\alpha$ and $\theta_{12}$ for various R values for the first $H^-$ $^1S$ hyperspherical channel $\mu = 1$. (From Ref. 53.)

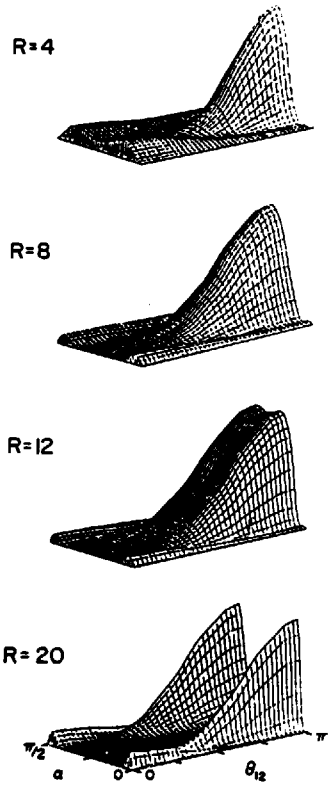


Fig. 15. Plot of $|\phi_\mu(R;\alpha,\theta_{12})|^2$ vs. $\alpha$ and $\theta_{12}$ for various R values for the second $H^-$ $^1S$ hyperspherical channel $\mu = 2$. (From Ref. 53.)

is the recent calculation of the photoionization plus excitation cross section of Be by Greene.[65]

Greene[65] has calculated the photoionization cross section of Be including coupling between the lowest two hyperspherical channels, $\mu = 1$ corresponding to leaving the ion in its ground 2s state and $\mu = 2$ corresponding to leaving the ion in its excited 2p state. (The inner $1s^2$ core was represented by a central potential so that

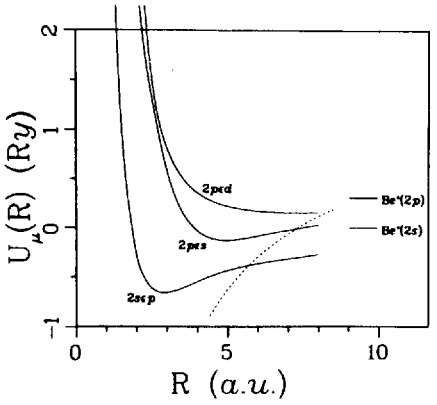


Fig. 17. Hyperspherical potential curves $-U_\mu(R)/R^2$ vs. R for the three Be $^1P$ channels converging to the n = 2 state of $Be^+$. (From Ref. 65.)

populated; it has a much less repulsive potential barrier than either the $\mu = 2$ or $\mu = 3$ channels. Macek[52] has shown that the hyperspherical adiabatic channel $\mu = 1$ corresponds to the 2sp+ channel of Cooper, Fano, and Prats[67] while $\mu = 2$ and $\mu = 3$ correspond to the 2sp- and 2pd channels respectively. The channel function $\phi_\mu$ for the "+" channel ($\mu$=1) is symmetric in $\alpha$ having an antinode on the potential ridge in Fig. 13 while the "-" channel ($\mu$=2) is antisymmetric in $\alpha$, having a node on the potential ridge. The symmetry about $\alpha = \pi/4$ for the He wavefunctions holds for all R values due to the degeneracy in energy of these channels. Note also that the "+" and "-" channels are shown to cross in Fig. 16. This crossing is actually avoided, but in any case the channel functions $\phi_\mu$ do not adjust to the crossing but proceed diabatically through it. For this reason the middle curve for $R > 7.5$ a.u. has "+" character while the lowest curve for $R > 7.5$ a.u. has "-" character.

Consider now the Be potentials in Fig. 17. Two differences from He are immediately apparent. First, the potential curves are

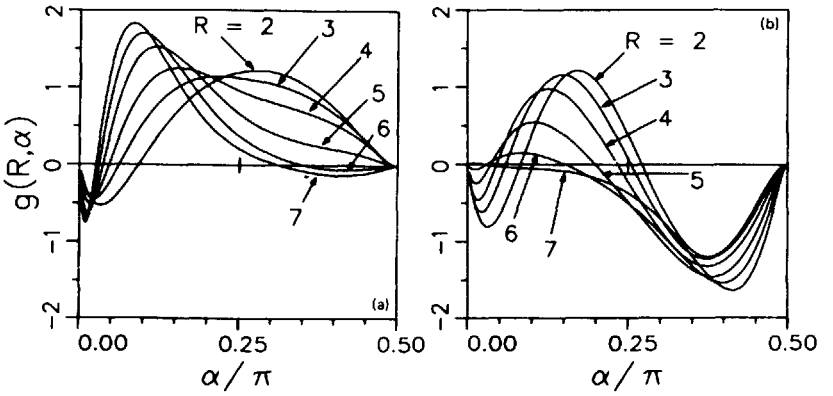


Fig. 18. Adiabatic "sp" channel wave functions associated with the lowest two Be potential curves: (a) $2s\varepsilon p$, $\mu = 1$; (b) $2p\varepsilon s$, $\mu = 2$. (From Ref. 65.)

non-degenerate for $R \to \infty$. Secondly there is an avoided crossing between the first and second potential curves for $4 \leqslant R \leqslant 6$. Otherwise, however, one expects most of the absorption strength, as in He, to go into the channel with the lowest potential curve. In his calculations Greene expanded the channel functions as follows:

$$\phi_\mu = \sum_{\ell_1\ell_2} g_\mu^{\ell_1\ell_2}(R;\alpha)\, Y_{\ell_1\ell_2 LM}(\hat{r}_1,\hat{r}_2) \tag{32}$$

The most important functions $g_\mu^{\ell_1\ell_2}$ (those with $\ell_1\ell_2$ = "sp") are shown in Fig. 18 for the potential curves $\mu = 1$ and $\mu = 2$ for various R values. For $R = 2$ one sees that the $\mu = 1$ function is approximately symmetric about $\alpha = \pi/4$ while the $\mu = 2$ function is approximately antisymmetric, just as for the "+" and "-" channels in He. As R increases, however, the channel functions drop into one or the other of the potential valleys in Fig. 13, i.e., the $\mu = 1$ amplitude becomes concentrated near $\alpha = 0$ while the $\mu = 2$ amplitude becomes concentrated near $\alpha = \pi/2$. Thus, as R increases

the non-degeneracy of the thresholds in Be causes a breakdown of the "+" and "-" symmetry about $\alpha = \pi/4$ observed at small R values. Furthermore this transition is seen to occur for R values $4 \leqslant R \leqslant 6$.

What is remarkable about Greene's solution of the radial equation (29) is that the solution that at small R starts out in the $\mu = 1$ channel as the adiabatic solution $F_{\mu=1}(R)\phi_{\mu=1}(R;\Omega)$ becomes at $R > 6$ a nearly equal superposition of the adiabatic solutions for $\mu = 1$ and $\mu = 2$ in such a way that the "+" symmetry is preserved through the avoided potential crossing region. In other words, just as in He, the "+" solution proceeds diabatically through the avoided potential crossing. This also explains the observed large excitation cross section seen in Be. Furthermore it is expected that this diabatic behavior of the hyperspherical "+" solution will be a common feature of all alkaline earth and other similar two electron systems.[65,68] This common feature of He and Be photoexcitation processes, despite vast differences in the coupling strength between the associated channels, is one of the most recent of the new perspectives on two-electron correlations provided by the hyperspherical coordinate method.

The Fock Expansion About R = 0

We return now to the question of the slow convergence of calculations which couple hyperspherical adiabatic channels. A clue to the difficulty is the observation that while the separable approximation in hyperspherical coordinates gives a very good initial approximation to the exact two electron wavefunction, it becomes inadequate for describing states of moderate and high kinetic energy relative to the bottom of the hyperspherical potential $U_\mu(R)$. If we consider the adiabatic potential curves for He and Be shown in Figs. 16 and 17 we see that at very small R these curves all have a strong generalized angular momentum barrier. For states lying at low energy E in the potential, the radial function $F_{\mu E}(R)$ is small for small R and is not significantly affected by this barrier. When E is sufficiently high, however, the radial wavefunction is repelled by the barrier and is accordingly shifted in phase. The so-called "post adiabatic" approximation has addressed this problem and obtains a faster convergent procedure, but only at the expense of a poorer first approximation at low energies.[69] Unpublished calculations for He[61] have shown that coupling between the adiabatic hyperspherical channels is strong near R = 0 and that series expansions of the radial solutions near R = 0 must incorporate powers of $\ell n R$ whenever coupling is introduced.

Fock[70] has shown that the full two-electron wavefunction has the following series expansion near R = 0:

$$\psi(\vec{r}_1,\vec{r}_2) = \sum_n \sum_m C_{nm}(\alpha,\hat{r}_1,\hat{r}_2)\, R^n(\ell nR)^m \qquad (33)$$

Demkov and Ermolaev[71] have generalized the Fock expansion in the hyperpherical coordinate R to an N-electron system having any symmetry. In addition, Macek[72] has proved that, for sufficiently small values of the mean square radius R of the two electrons, the Fock expansion converges and thus does indeed represent a physical solution. The numerical calculations[61] indicate that the $\ell nR$ terms are inextricably linked with the coupling of adiabatic hyperspherical solutions near R = 0. Since the Fock expansion in Eq. (33) is an exact solution of the problem, it must be that the full expansion treats all coupling between the adiabatic channels. Such coupling is necessary to reduce the effect of the excessive repulsion of the centrifugal potential barrier within the individual adiabatic hyperspherical channels.

Given the numerical difficulties near R = 0 when representing the two-electron wavefunctions as an expansion in adiabatic channel functions, as in Eq. (27), it makes sense to simply use the exact Fock expansion in Eq. (33) near R = 0. One still has the nontrivial task of calculating the coefficients $C_{nm}$ in Eq. (33), of course. Given such an expansion as in Eq. (33), however, one could match onto an expansion in terms of a few adiabatic hyperspherical channel functions, as in Eq. (27), at some radius $R = R_0$ near the bottom of the potential curves $-U_\mu(R)/R^2$ (cf. Figs. 16 and 17) well away from the troublesome centrifugal barrier region near R = 0. The precise method of matching the solutions in the two regions must also be developed. One hopes, of course, that once the wavefunction is obtained for $R < R_0$ that the expansion in hyperspherical adiabatic solutions will be rapidly convergent. This hyperspherical R-matrix method using the Fock expansion in the inner $R < R_0$ region is being carried out collaboratively by Joseph Macek, the author, and co-workers at the University of Nebraska.

## CONCLUDING REMARKS

We have reviewed here in a compact way current theoretical understanding of the photoionization process. Single electron photoionization processes are generally well understood, at least for closed-shell atoms, in terms of the effects of the so-called particle-hole electron correlations. Even so, in regions of small cross sections such as near cross section minima, relativistic and other weak interactions play an important rôle. Real two-electron

photoexcitation processes are attracting increasing experimental and theoretical interest and we have described here one theory, the hyperspherical coordinate method, which has provided a number of insights into the important correlations involved and which is still under very active development.

Finally, it should be stressed that although we have focused here on photoionization cross sections, it is becoming increasingly important for theoreticians to present their results in the form of transition amplitudes and phases. In the first place one needs such theoretical data to predict other aspects of the photoionization process, such as photoelectron angular distributions, and photoelectron spin polarizations. Secondly, there are a growing number of so-called "complete" experiments[73-75] which use data obtained from cross sections, angular distributions, and photoelectron spin polarizations to provide experimental values for the transition amplitudes and phases. Thirdly, as shown by Flügge et al.,[76] the photoionization process produces an alignment of the residual ion. This alignment may be observed experimentally by measuring the polarization of the subsequent fluorescence radiation or else the angular distribution of the subsequent Auger electrons. The alignment itself, however, is calculated theoretically using the dipole amplitudes for the photoionization process. The day is thus approaching when experimentalists and theoreticians will each present their results in the form of the fundamental dynamical amplitudes of the collision process under study. Such comparisons will provide very stringent tests of theoretical understanding of the photoionization process since transition amplitudes and phases are usually much more sensitive to electron correlation and other effects than are the photoionization cross sections.

REFERENCES

1. A. F. Starace, "Theory of Atomic Photoionization," in Handbuch der Physik, Vol. 31, W. Mehlhorn, Ed. (Springer, Berlin, 1982). pp 1-121.
2. A. F. Starace, "Trends in the Theory of Atomic Photoionization," Applied Optics 19, 4051-4062 (1980).
3. A. F. Starace, "New Perspectives on Electron Correlations," in Physics of Electronic and Atomic Collisions, S. Datz, Ed. (North-Holland, Amsterdam, 1982), pp 431-446.
4. J. J. Sakurai, Advanced Quantum Mechanics (Addison-Wesley, Reading, Massachusetts, 1967), p. 39.
5. S. Chandrasekhar, Astrophys. J. 102, 223 (1945).
6. A. F. Starace, Phys. Rev. A 3, 1242 (1971); 8, 1141 (1973).
7. M. Ya Amusia and N. A. Cherepkov, "Many-Electron Correlations in Scattering Processes," Case Studies in Atomic Physics 5, 47 (1975).
8. J. M. Blatt and L. C. Biedenharn, Rev. Mod. Phys. 24, 258 (1952).

9. C. N. Yang, Phys. Rev. 74, 764 (1948).
10. D. J. Botto, J. McEnnan, R. H. Pratt, Phys. Rev. A 18, 580 (1978).
11. R. H. Pratt, A. Ron and H. K. Tseng, Rev. Mod. Phys. 45, 273 (1973).
12. E. Storm and H. I. Israel, Nucl. Data Tables A 7, 565 (1970).
13. J. H. Scofield, Lawrence Livermore Laboratory Report No. UCRL-51326 (1973).
14. S. D. Oh, J. McEnnan, and R. H. Pratt, Phys. Rev. A 14, 1428 (1976).
15. H. A. Bethe and E. E. Salpeter, Quantum Mechanics of One- and Two-Electron Atoms (Springer, Berlin, 1957), Sections 69-71.
16. D. J. Kennedy and S. T. Manson, Phys. Rev. A 5, 227 (1972).
17. J. W. Cooper, Phys. Rev. 128, 681 (1962).
18. U. Fano and J. W. Cooper, Rev. Mod. Phys. 40, 441 (1968), Section 4.
19. M. Goeppert-Mayer, Phys. Rev. 60, 184 (1941).
20. A. R. P. Rau and U. Fano, Phys. Rev. 167, 7 (1968).
21. F. Herman and S. Skillman, Atomic Structure Calculations (Prentice-Hall, Englewood Cliffs, New Jersey, 1963).
22. D. R. Bates, Mon. Not. Roy. Astron. Soc. 106, 432 (1946).
23. M. J. Seaton, Proc. Roy. Soc. A 208, 418 (1951).
24. A. Msezane and S. T. Manson, Phys. Rev. Lett. 35, 364 (1975).
25. Y. S. Kim, A. Ron, R. H. Pratt, B. R. Tambe, and S. T. Manson, Phys. Rev. Lett. 46, 1326 (1981).
26. Y. S. Kim, R. H. Pratt, and A. Ron, Phys. Rev. A 24, 1626 (1981).
27. A. Z. Msezane and S. T. Manson, Phys. Rev. Lett. 48, 473 (1982).
28. M. J. Seaton, C. R. Acad. Sci. 240, 1317 (1955); Mon. Not. Roy. Astron. Soc. 118, 504 (1958).
29. S. T. Manson and A. F. Starace, Rev. Mod. Phys. 54, 389 (1982).
30. M. S. Wang, Y. S. Kim, R. H. Pratt, and A. Ron, Phys. Rev. A 25, 857 (1982).
31. A. F. Starace, Phys. Rev. A 2, 118 (1970).
32. J. A. R. Samson, Adv. At. Mol. Phys. 2, 177 (1966).
33. L. Lipsky and J. W. Cooper (unpublished). Results presented in Fig. 22 of Ref. 18.
34. T. N. Chang, Phys. Rev. A 15, 2392 (1977).
35. H. P. Kelly and R. L. Simons, Phys. Rev. Lett. 30, 529 (1973).
36. R. P. Madden, D. L. Ederer, and K. Codling, Phys. Rev. 177, 136 (1969).
37. P. G. Burke and K. T. Taylor, J. Phys. B 8, 2620 (1975).
38. M. Ya Amusia, V. K. Ivanov, N. A. Cherepkov, and L. V. Chernysheva, Phys. Lett. A 40, 361 (1972).
39. C. D. Lin, Phys. Rev. A 9, 181 (1974).
40. J. A. R. Samson and J. Gardner, Phys. Rev. Lett. 33, 671 (1974).

41. R. G. Houlgate, J. B. West, K. Codling, and G. V. Marr, J. Electron Spectrosc. Relat. Phenom. 9, 205 (1976).
42. G. Wendin, in Photoionization and Other Probes of Many-Electron Interactions, F. J. Wuilleumier, Ed. (Plenum, New York, 1976), pp. 61-82.
43. H. P. Kelly, in Photoionization and Other Probes of Many-Electron Interactions, F. J. Wuilleumier, Ed. (Plenum, New York, 1976), pp. 83-110.
44. P. G. Burke and W. D. Robb, Adv. At. Mol. Phys. 11, 143 (1975).
45. T. N. Chang and U. Fano, Phys. Rev. A 13, 263, 282 (1976).
46. J. R. Swanson and L. Armstrong, Jr., Phys. Rev. A 15, 661 (1977); 16, 1117 (1977).
47. W. R. Johnson and C. D. Lin, Phys. Rev. A 20, 964 (1979).
48. W. R. Johnson and K. T. Cheng, Phys. Rev. A 20, 978 (1979).
49. K.-N. Huang, W. R. Johnson, and K. T. Cheng, Phys. Rev. Lett. 43, 1658 (1979).
50. N. A. Cherepkov and L. V. Chernysheva, Phys. Lett. A 60, 103 (1977).
51. A. F. Starace and S. Shahabi, Phys. Rev. A 25, 2135 (1982).
52. J. H. Macek, J. Phys. B 2, 831 (1968).
53. C. D. Lin, Phys. Rev. A 25, 76 (1982); "Comparison of Configuration-Interaction Wave Functions with Adiabatic Channel Functions in Hyperspherical Coordinates," Phys. Rev. A (in press).
54. C. D. Lin, Phys. Rev. A 10, 1986 (1974).
55. C. D. Lin, Phys. Rev. Lett. 35, 1150 (1975); Phys. Rev. A 14, 30 (1976).
56. C. H. Greene, J. Phys. B 13, L39 (1980).
57. C. D. Lin, Phys. Rev. A 12, 493 (1975).
58. D. L. Miller and A. F. Starace, J. Phys. B 13, L525 (1980).
59. J. A. R. Samson, Phys. Reports 28C, 303 (1976).
60. V. L. Jacobs, Phys. Rev. A 3, 289 (1971).
61. D. L. Miller and A. F. Starace (unpublished).
62. U. Fano, Phys. Rev. A 22, 2660 (1980).
63. C. D. Lin, Phys. Rev. A 10, 1986 (1974).
64. (a) G. Wannier, Phys. Rev. 90, 817 (1953).
(b) R. Peterkop, J. Phys. B 4, 513 (1971).
(c) A. R. P. Rau, Phys. Rev. A 4, 207 (1971).
65. C. H. Greene, Phys. Rev. A 23, 661 (1981).
66. J. Dubau and J. Wells, J. Phys. B 6, 1452 (1973).
67. J. W. Cooper, U. Fano, and F. Prats, Phys. Rev. Lett. 10, 518 (1963).
68. U. Fano, Physica Scripta 24, 656 (1981).
69. H. Klar and U. Fano, Phys. Rev. Lett. 37, 1132 (1976); H. Klar, Phys. Rev. A 15, 1452 (1977); H. Klar and M. Klar, Phys. Rev. A 17, 1007 (1978).

70. V. Fock, Izvest. Acad. Nauk USSR ser Fiz. 18, (1954) [Eng. Transl.: Kong. Norske Videnskabers Selskabs Forh. 31, 138, 145 (1958).]
71. Yu. N. Demkov and A. M. Ermolaev, Zh. Eksp. Teor. Fiz. 36, 896 (1959) [Sov. Phys. -JETP 36, 633 (1969)].
72. J. H. Macek, Phys. Rev. 160, 170 (1967).
73. J. Kessler, "The 'Perfect' Photoionization Experiment," Comments Atom. Mol. Phys. 10, 47 (1981). See also references to earlier work therein.
74. U. Heinzmann, J. Phys. B 13, 4353 (1980); 13, 4367 (1980).
75. F. Schäfers, G. Schönhense, and U. Heinzmann, "Experimental Determination of Matrix Elements and Phase Difference for Hg $6s^2$ Photoionization," XII Int'l. Conf. Phys. Elec. Atom. Coll., Gatlinburg, Tenn., 1981, Abstracts Vol. 1, p. 5.
76. S. Flügge, W. Mehlhorn, and V. Schmidt, Phys. Rev. Lett. 29, 7 (1972).

ACKNOWLEDGMENT

The author gratefully acknowledges the research support of the U. S. Department of Energy and the U. S. National Science Foundation.